Ejecta from the DART-produced active asteroid Dimorphos

Jian-Yang Li (jyli@psi.edu)
Planetary Science Institute https://orcid.org/0000-0003-3841-9977

Masatoshi Hirabayashi
Auburn University

Tony Farnham
University of Maryland College Park

Matthew Knight
United States Naval Academy

Gonzalo Tancredi
Facultad Ciencias https://orcid.org/0000-0002-4943-8623

Fernando Moreno
Instituto de Astrofísica de Andalucía, CSIC, Glorieta de la Astronomía

Brian Murphy
University of Edinburgh, Royal Observatory

Cyrielle Opitom
University of Edinburgh

Steven Chesley
Jet Propulsion Laboratory

Jessica Sunshine
University of Maryland

Daniel Scheeres
University of Colorado Boulder https://orcid.org/0000-0003-0558-3842

Cristina Thomas
Northern Arizona University https://orcid.org/0000-0003-3091-5757

Eugene Fahnestock
Jet Propulsion Laboratory, California Institute of Technology

Andrew Cheng
Johns Hopkins University https://orcid.org/0000-0001-5375-4250

Linda Dressel
Space Telescope Science Institute

Carolyn Ernst
Johns Hopkins University Applied Physics Laboratory

Fabio Ferrari

Politecnico di Milano

Alan Fitzsimmons

Queen's University Belfast https://orcid.org/0000-0003-0250-9911

Simone Ieva

INAF-Osservatorio Astronomico di Roma

Stavro Ivanovski

INAF - Osservatorio Astronomico di Trieste

Teddy Kareta

Lowell Observatory

Ludmilla Kolokolova

Department of Astronomy, University of Maryland

Tim Lister

Las Cumbres Observatory

Sabina Raducan

University of Bern https://orcid.org/0000-0002-7478-0148

Andrew Rivkin

Johns Hopkins University Applied Physics Laboratory https://orcid.org/0000-0002-9939-9976

Alessandro Rossi

IFAC-CNR https://orcid.org/0000-0001-9311-2869

Stefania Soldini

Department of Mechanical, Materials and Aerospace Engineering, University of Liverpool

Angela Stickle

Johns Hopkins University Applied Physics Laboratory

Alison Vick

Space Telescope Science Institute

Jean-Baptiste Vincent

Deutsches Zentrum für Luft- und Raumfahrt (DLR), Institut für Planetenforschung

Harold Weaver

The Johns Hopkins University Applied Physics Laboratory https://orcid.org/0000-0003-0951-7762

Stefano Bagnulo

Armagh Observatory and Planetarium https://orcid.org/0000-0002-7156-8029

Michele Bannister

School of Physical and Chemical Sciences — Te Kura Matū, University of Canterbury

Saverio Cambioni

Massachusetts Institute of Technology

Adriano Campo Bagatin

University of Alicante https://orcid.org/0000-0001-9840-2216

Nancy Chabot

Johns Hopkins University Applied Physics Laboratory https://orcid.org/0000-0001-8628-3176

Gabriele Cremonese
INAF, Osservatorio Astronomico di Padova
Ronald Daly
Johns Hopkins University Applied Physics Laboratory https://orcid.org/0000-0002-1320-2985
Elisabetta Dotto
INAF-Osservatorio Astronomico di Roma
David Glenar
Center for Space Science and Technology, University of Maryland
Mikael Granvik
University of Helsinki https://orcid.org/0000-0002-5624-1888
Pedro Hasselmann
INAF-Osservatorio Astronomico di Roma
M. Herreros
Centro de Astrobiología (CSIC-INTA) https://orcid.org/0000-0001-5284-8060
Seth Jacobson
Michigan State University https://orcid.org/0000-0002-4952-9007
Martin Jutzi
University of Bern
Tomas Kohout
University of Helsinki https://orcid.org/0000-0003-4458-3650
Fiorangela La Forgia
Department of Physics and Astronomy University of Padova https://orcid.org/0000-0003-3924-1867
Monica Lazzarin
University of Padova
Zhong-Yi Lin
24National Central University, Graduate Institute of Astronomy
Ramin Lolachi
Center for Space Science and Technology, University of Maryland at Baltimore County
Alice Lucchetti
Osservatorio Astronomico di Padova https://orcid.org/0000-0001-7413-3058
Rahil Makadia
University of Illinois at Urbana-Champaign https://orcid.org/0000-0001-9265-2230
Elena Mazzotta Epifani
INAF-Osservatorio Astronomico di Roma
Patrick Michel
Université Côte d'Azur, Observatoire de la Côte d'Azur, CNRS, Laboratoire Lagrange
https://orcid.org/0000-0002-0884-1993
Alessandra Migliorini
INAF - Institute of Space Astrophysics and Planetology

Nicholas Moskovitz
Lowell Observatory
Jens Ormö
Centro de Astrobiología (CSIC-INTA)
Maurizio Pajola
INAF - Astronomical Observatory of Padova https://orcid.org/0000-0002-3144-1277
Paul Sánchez
University of Colorado Boulder https://orcid.org/0000-0003-3610-5480
Stephen Schwartz
Planetary Science Institute
Colin Snodgrass
University of Edinburgh https://orcid.org/0000-0001-9328-2905
Jordan Steckloff
Planetary Science Institute
Timothy Stubbs
NASA Goddard Space Flight Center
Josep Trigo-Rodríguez
Institute of Space Sciences

Physical Sciences - Article

Keywords:

Posted Date: November 22nd, 2022

DOI: https://doi.org/10.21203/rs.3.rs-2292349/v1

Version of Record: A version of this preprint was published at Nature on March 1st, 2023. See the published version at https://doi.org/10.1038/s41586-023-05811-4.

Abstract

NASA's Double Asteroid Redirection Test (DART) mission performed the first ever kinetic impact to deflect an asteroid[1]. The DART kinetic impact test artificially activated an asteroid with a hypervelocity impact, providing a unique opportunity for an extensive observing campaign to monitor the evolutionary process from the formation of the ejecta to its dispersion via a sustained tail. Here we report observations of the impact ejecta with the Hubble Space Telescope (HST) from impact time (T)+15 minutes to T+18.5 days at a resolution of 2.1 km per pixel. Our observations showed that the gravitational interaction between the binary system and dust under the influence of solar radiation pressure produced a complex morphology during the evolution of the ejecta. The dust ejected at speeds much higher than the escape speed of the binary system (0.25 m/s) is directly ejected out of the system. The dust moving at speeds just above the escape speed displayed signatures of gravitational interaction with the binary asteroid system, forming spirals and extended features. Slow ejecta is ultimately pushed in the antisolar direction (nearly opposite the impact direction) by solar radiation pressure to form a tail. These dynamical processes are highly dependent on particle size and ejection direction. The ejecta evolution following DART's kinetic impact offers a framework for understanding the fundamental mechanisms acting on asteroids disrupted by natural impact[2,3] for the first time.

Introduction

HST observed the ejecta once every 1.6 hours during the first 8 hours after DART's impact (Extended Data Table 1) at a viewing geometry shown in Fig. 1. The image collected at about T+0.4 hour (Fig. 2a) shows diffuse ejecta with several linear structures and clumps spanning nearly the entire eastern hemisphere. After ~T+2 hours, the initial, diffuse dust cloud had mostly dissipated. An overall cone-shaped ejecta morphology emerged with many structural features (Fig. 2b – 2f). Some features are visible in multiple images and extended to nearly 500 km from the asteroid. The motion of these features, expanding radially away from the asteroid at constant speeds between a few and ~30 m/s as projected in the sky (Extended Data Table 2), suggests that they are directly ejected out of the Didymos system without being appreciably influenced by the gravity of the system or by solar radiation pressure. Based on the position angles (angle measured from north toward east) of the cone and a simple model (Methods), we find that the observed ejecta cone is consistent with a 3D opening angle of 130º±10º and centerline at a position angle of 67±8º, almost parallel to the incoming direction of the DART spacecraft.

Dimorphos's ejecta was distinctive from the ejecta of Comet 9P/Tempel 1 produced by the only previous planetary impact experiment, Deep Impact[4] (Extended Data Figure 1a – 1c). Also observed by HST, the Deep Impact ejecta was diffuse and mostly featureless, expanding at an average speed of ~100 m/s and a maximum speed of ~300 m/s[5,6]. The different ejecta morphology is attributed to the different target compositions and subsurface structures. While Tempel 1 has a highly porous subsurface[7] composed of fine-grained dust and rich in volatiles[8,9], Dimorphos has a bouldery surface and a rubble-pile interior[1].

At ~T+18 hours, two bright spiral features, together with some new, fainter, and smaller linear features in between, were apparent at the base of the original cone (s1, s2; see Fig. 3a). The northern and southern spirals had distinctly different morphologies and evolution. The northern spiral had an 18º counter-clockwise offset from the northern edge of the ejecta cone and continuously shifted toward the antisolar direction. After T+3 days, it started to show increasing widening along the antisolar direction, with a diffuse anti-sunward edge and a relatively sharp sunward edge, forming a wing-like shape and continuously fading after T+4.7 days (Fig. 3f – 3j). In contrast, the southern spiral started within 5º of the southern edge of the ejecta cone, and its spiral motion was smaller and more gradual than the northern spiral (Fig. 3a – 3d). As time passed, the southern spiral moved clockwise, in the same direction as the orbital motion of Dimorphos around Didymos at the time of impact. Starting from T+4.7 days, the tip of the southern spiral split into a few linear features (l21 – l24), which subsequently extended toward the antisolar direction to align with the tail (Fig. 3f – 3i). Some of them (l20, l22) expanded in the sunward direction to the maximum distances of 150 – 200 km after 10 days (Fig. 2i) before retreating towards the tail direction and finally fading out. In addition, the small linear features (l16 – l19) between the two spirals behaved similarly to the southern spiral, extending to the north of Didymos and toward the tail direction, forming lineaments overlaid with the wing-like structure (Fig. 3c – 3i).

The complex morphology evolution of the spirals and linear features indicates gravitational interaction between the ejecta particles and Didymos. The hyperbolic excess speeds of these particles are <0.3 m/s, indicating their initial speeds were within twice the system escape speed (~0.25 m/s). From the Earth-observing geometry (Fig. 1), particles launched toward Didymos would predominantly appear in the northern spiral, whereas the southern spiral contains more particles launched away from Didymos. Pre-impact numerical simulations[10-14] predicted an asymmetric behavior for particles launched inward and outward of the orbit of Dimorphos. Particles launched inward would be accelerated and their trajectories bent by Didymos before leaving the system, forming the observed northern spiral with the end nearest Didymos shifted. Particles launched outward would directly depart from the binary system, more or less along the radial direction. This interpretation appears consistent with the observed structure.

Beyond the gravitational influence of the Didymos system, solar radiation pressure would separate particles of different sizes along the sunward-antisunward direction, with small particles being accelerated faster than large particles[15]. Situated roughly orthogonal to the sunward direction, the northern spiral was widened to the observed wing shape, with particle size sorted along the sunward-antisunward direction and speed roughly sorted along the orthogonal direction. Its abrupt sunward edge indicates a cutoff in the largest particle size in the ejecta. The southern spiral is more aligned toward the sun, and those particles are decelerated and eventually forced to loop backward. Any clumps of particles will spread out, forming the series of observed linear features extending in the antisunward direction (l16 – l24). The finer particles in feature l16 – l18 are pushed further and caught up to the larger particles ejected into the northern spiral earlier, appearing to overlap with the wing-like structure and creating a more complex pattern.

A dust tail started to emerge anti-sunward nearly opposite the ejecta cone at ~T+3 hours, and quickly stretched out to >1500 km projected length and exceeded the spatial coverage of our images (Fig. 4). The tail is a result of solar radiation pressure. Around T+5.7 days, the narrow tail showed a relatively bright and sharp southern edge and a parallel but more diffuse northern edge (Fig. 4h). The overall morphology of Dimorphos's tail is similar to that of P/2010 A2, an active asteroid likely triggered by impact[16-20] (Extended Data Figure. 1d, 1e). The ~1" width of the tail is consistent with an initial speed of the dust comparable to the orbital speed of Dimorphos, suggesting that the tail contains the slowest ejecta particles. Additionally, the early tail within T+2 days slightly curved towards the south (Fig. 4d, 4e), whereas after T+8 days the tail became slightly more fan-shaped (Fig. 4i – 4k). With radiation pressure sorting out particle size along the tail, the brightness profile of the tail is related to the differential size frequency distribution in the ejecta. We find that the particle size in the portion of the tail in the HST field of view progressively increased from about 1 μm initially to a few cm in the last HST image. Assuming a power law size frequency distribution, we derived an exponent of -2.6±0.2 for particles of 1 μm – a few mm radius, and an exponent of -3.6±0.2 for larger particles up to a few cm (Extended Data Fig. 5). Ejecta particles are observed to continuously leave the Didymos system through the final images acquired after T+15 days (Extended Data Figs. 2, 3).

Additionally, a secondary tail appeared between T+5.7 and T+8.8 days (Fig. 4i – 4k) but was no longer discernible on T+18.5 days (Fig. 4l). It originated from the Didymos system and pointed about 4º further north of the original tail, creating an overall fan-shaped tail morphology during this timeframe. The cause of the secondary tail is unclear. Multiple mechanisms are to be explored, although evidence exists to support a secondary dust emission as the source of the secondary tail (Methods, Extended Data Figs. 2, 6), consistent with the previous observations of active asteroids that displayed multiple tails[21-24].

The DART ejecta has implications about the near-surface structure of Dimorphos, and can be used to infer the kinetic impact momentum transfer efficiency independent of the observed period change of Dimorphos[25,26]. More importantly, the DART mission showed definitively that impacts can activate asteroids consistent with prior asteroid observations[1]. Our observations provided a basis for reassessing the previous observations of active asteroids thought to be triggered by impact, including P/2010 A2[16-20] and (596) Scheila[27-29]. The evolution of Dimorphos's ejecta suggests that an observational selection effect could have contributed to the observed mm- to cm-sized dust for P/2010 A2[16,18], consistent with the largest particle size found in Dimorphos's ejecta. In contrast, ejecta from Scheila was dominated by μm-sized particles traveling at speeds up to 100 m/s, and the quick fading of ejecta indicated a lack of particles >10 μm[27]. This can be explained since Scheila was observed as soon as one week after the impact when small particles were still present, whereas the ejecta of P/2010 A2 was first observed 10 months after impact when small particles likely have been cleared. DART, as a controlled, planetary-scale impact experiment, provides a detailed characterization of the target, the ejecta morphology, and the entire ejecta evolution process. DART will continue to be the model for studies of newly discovered asteroids that are activated by natural impacts.

References

1. Daly, R.T., et al. DART: An Autonomous kinetic impact into a near-Earth asteroid for planetary defense. *Nature*, **this issue** (2022).
2. Jewitt, D. & Hsieh, H. H. The Asteroid-Comet Continuum, arXiv:2203.01397. Preprint at https://arxiv.org/abs/2203.01397 (2022).
3. Tancredi, G., Liu, P.-Y., Campo-Bagatin, A. Moreno, F. & Domínguez, B. Lofting of low speed ejecta produced in the DART experiment and production of a dust cloud, *Monthly Notices of the Royal Astronomical Society*, stac3258, doi:10.1093/mnras/stac3258. https://doi.org/10.1093/mnras/stac3258 (2022).
4. A'Hearn, M. F., Belton, J. S., Delamere, W. A., Kissel, J., Klaasen, K. P. et al. Deep Impact: Excavating Comet Tempel 1, *Science*, **310**, 5787, 635-640, doi:10.1126/science.1118923, https://doi.org/10.1126/science.1118923 (2005).
5. Feldman, P.D., McCandliss, S.R., Route, M., Weaver, H.A., A'Hearn, M.F., Belton, M.J.S., Meech, K.J. Hubble Space Telescope Observations of Comet 9P/Tempel 1 during the Deep Impact encounter. Icarus, **187**, 113-122. doi:10.1016/j.icarus.2006.07.027. https://doi.org/10.1016/j.icarus.2006.07.027 (2007).
6. Meech, K. J., Ageorges, N., A'Hearn, M. F., Arpigny, C., Ates, A. et al. Deep Impact: Observations from a Worldwide Earth-Based Campaign, *Science*, **310**, 5746, 265-269, doi:10.1126/science.1118978. https://doi.org/10.1126/science.1118978 (2005).
7. Richardson, J.E., Melosh, H.J., Lisse, C.M., Carcich, B. A ballistics analysis of the Deep Impact ejecta plume: Determining Comet Tempel 1's gravity, mass, and density. *Icarus*, **190**, 357-390, doi: 10.1016/j.icarus.2007.08.001. https://doi.org/10.1016/j.icarus.2007.08.001 (2007).
8. Sunshine, J.M., Groussin, O., Schultz, P.H., A'Hearn, M.F., Feaga, L.M., Farnham, T.L., Klaasen, K.P. The distribution of water ice in the interior of Comet Tempel 1. *Icarus*, **190**, 284-294, doi: 10.1016/j.icarus.2007.04.024. https://doi.org/10.1016/j.icarus.2007.04.024 (2007).
9. Lisse, C.M., VanCleve, J., Adams, A.C., A'Hearn, M.F., Fernández, Y.R., et al. Spitzer spectral observations of the Deep Impact Ejecta. *Science*, **313**, 635-640, doi: 10.1126/science.1124694. https://doi.org/10.1126/science.1124694 (2006).
10. Moreno, F., Campo Bagatin, A., Tancredi, G., Liu, P.-Y. & Domínguez, B. Ground-based observability of Dimorphos DART impact ejecta: photometric predictions, Monthly Notices of the Royal Astronomical Society, 515, 2, 2178-2187, doi:10.1093/mnras/stac1849. https://doi.org/10.1093/mnras/stac1849 (2022).
11. Ferrari, F., Raducan, S. D., Soldini, S. & Jutzi, M. Ejecta Formation, Early Collisional Processes, and Dynamical Evolution after the DART Impact on Dimorphos. *The Planetary Science Journal*, **3**, 177, doi:10.3847/PSJ/ac7cf0. https://doi.org/10.3847/PSJ/ac7cf0 (2022).
12. Rossi, A., Marzari, F., Brucato, J. R., Della Corte, V., Dotto, E. et al. Dynamical Evolution of Ejecta from the DART Impact on Dimorphos, The Planetary Science Journal, **3**, 118, doi:10.3847/PSJ/ac686c,

https://doi.org/10.3847/PSJ/ac686c (2022).

13. Yu, Y., Michel, P., Schwartz, S. R., Naidu, S. P. & Benner, L. A. M. Ejecta Cloud from the AIDA Space Project Kinetic Impact on the Secondary of a Binary Asteroid: I. Mechanical Environment and Dynamical Model. *Icarus*, **282**, 313-325, doi:10.1016/j.icarus.2016.09.008. https://doi.org/10.1016/j.icarus.2016.09.008 (2017).
14. Yu, Y. & Michel, P. Ejecta cloud from the AIDA space project kinetic impact on the secondary of a binary asteroid: II. fates and evolutionary dependencies. *Icarus*, **312**, 128-144, https://doi.org/10.1016/j.icarus.2018.04.017 (2018).
15. Burns, J. A., Lamy, P. L. & Soter, S. Radiation forces on small particles in the solar system, *Icarus*, **40**, 1, 1-48, doi:10.1016/0019-1035(79)90050-2, https://doi.org/10.1016/0019-1035(79)90050-2 (1979).
16. Jewitt, D., Weaver, H., Agarwal, J., Mutchler, M. & Druhus, M. A recent disruption of the main-belt asteroid P/2010 A2. *Nature*, **467**, 817-819, doi:10.1038/nature09456. https://doi.org/10.1038/nature09456 (2010).
17. Moreno, F., Licandro, J., Tozzi, G.-P., Ortiz, J. L. & Cabrera-Lavers, A. et al. WATER-ICE-DRIVEN ACTIVITY ON MAIN-BELT COMET P/2010 A2 (LINEAR)? *The Astrophysical Journal Letters*, **718**, L132-L136, doi:10.1088/2041-8205/718/2/L132. https://doi.org/10.1088/2041-8205/718/2/L132 (2010).
18. Snodgrass, C., Tubiana, C., Vincent, J. B., Sierks, H. & Hviid, S. et al. A collision in 2009 as the origin of the debris trail of asteroid P/2010 A2. *Nature*, **467**, 814–816, doi:10.1038/nature09453. https://doi.org/10.1038/nature09453 (2010)
19. Jewitt, D., Ishiguro, M. & Agarwal, J. LARGE PARTICLES IN ACTIVE ASTEROID P/2010 A2, *The Astrophysical Journal Letters*, **764**, L5, doi:10.1088/2041-8205/764/1/L5, http://dx.doi.org/10.1088/2041-8205/764/1/L5 (2013).
20. Hainaut, O. R., Kleyna, J., Sarid, G., Hermalyn, B. & Zenn, A. et al. P/2010 A2 LINEAR: I. An impact in the asteroid main belt. *Astronomy & Astrophysics*, A69, doi:10.1051/0004-6361/201118147. https://doi.org/10.1051/0004-6361/201118147 (2012).
21. Jewitt, D., Agarwal, J., Weaver, H., Mutchler, M. & Larson, S. THE EXTRAORDINARY MULTI-TAILED MAIN-BELT COMET P/2013 P5, *The Astrophysical Journal Letters*, **778**, L21, doi:10.1088/2041-8205/778/L21. http://dx.doi.org/10.1088/2041-8205/778/1/L21 (2013).
22. Jewitt, D., Agarwal, J., Weaver, H., Mutchler, M & Larson, S. EPISODIC EJECTION FROM ACTIVE ASTEROID 311P/PANSTARRS, The Astrophysical Journal, 798, 109, doi:10.1088/0004-637X/798/2/109. http://dx.doi.org/10.1088/0004-637X/798/2/109 (2015).
23. Jewitt, D., Weaver, H., Mutchler, M., Li, J., Agarwal, J. & Larson, S. The Nucleus of Active Asteroid 311P/(2013P5) PANSTARRS, *The Astronomical Journal*, **155**, 231. doi:10.3847/1538-3881/aabdee. https://doi.org/10.3847/1538-3881/aabdee (2018).
24. Jewitt, D., Kim, Y., Luu, J., Rajagopal, J., Kotulla & R. et al. Episodically Active Asteroid 6478 Gault, *The* Astrophysical *Journal Letters*, **876**, L19, doi:10.3847/2041-8213/ab1be8, https://doi.org/10.3847/2041-8213/ab1be8 (2019).

25. Thomas, C.A., Nadu, S.P., Scheirich, P., Moskovitz, N.A., Pravec, P., et al. Orbital period change of Dimorphos due to the DART kinetic impact. *Nature*, **this issue** (2022).
26. Cheng. A.F. et al. Momentum transfer from the DART mission kinetic impact on asteroid Dimorphos. *Nature*, **this issue** (2022).
27. Jewitt, D., Weaver, H., Mutchler, M., Larson, S. & Agarwal, J. *HUBBLE SPACE TELESCOPE* OBSERVATIONS OF MAIN-BELT COMET (596) SCHEILA, *The Astrophysical Journal Letters*, **733**, L4, doi:10.1088/2041-8205/733/1/L4. https://doi.org/10.1088/2041-8205/733/1/L4 (2011).
28. Ishiguro, M., Hanayama, H., Hasegawa, S., Sarugaku, Y., Watanabe, J. et al. OBSERVATIONAL EVIDENCE FOR AN IMPACT ON THE MAIN-BELT ASTEROID (596) SCHEILA, *The Astrophysical Journal Letters*, **740**, L11, doi:10.1088/2041-8205/740/1/L11. https://doi.org/10.1088/2041-8205/740/1/L11 (2011).
29. Bodewits, D., Kelley, M. S., Li, J.-Y., Landsman, W. B., Besse, S. et al. COLLISIONAL EXCAVATION OF ASTEROID (596) SCHEILA, *The Astrophysical Journal Letters*, **733**, L3, doi:10.1088/2041-8205/733/1/L3. https://doi.org/10.1088/2041-8205/733/1/L3 (2011).

Declarations

Acknowledgements This work was supported by the DART mission, NASA Contract No. 80MSFC20D0004 and by the Italian Space Agency (ASI) within the LICIACube project (ASI-INAF agreement AC n. 2019-31-HH.0). J.-Y.L. acknowledges the support provided by NASA through grant HST-GO-16674 from the Space Telescope Science Institute, which is operated by the Association of Universities for Research in Astronomy, Inc., under NASA contract NAS 5-26555. L.K. acknowledges support from NASA DART Participating Scientist Program, Grant #80NSSC21K1131. R.L., D.A.G., and T.J.S. acknowledge funding from the NASA/GSFC Internal Scientist Funding Model (ISFM) Exospheres, Ionospheres, Magnetospheres Modeling (EIMM) team, the NASA Solar System Exploration Research Virtual Institute (SSERVI), and NASA award number 80GSFC21M0002. R.M. acknowledges support from a NASA Space Technology Graduate Research Opportunities (NSTGRO) Award (Contract No. 80NSSC22K1173). P.M. acknowledges funding support from the European Union's Horizon 2020 research and innovation program under grant agreement No. 870377 (project NEO-MAPP), the CNRS through the MITI interdisciplinary programs, CNES and ESA. F.F. acknowledges funding from the Swiss National Science Foundation (SNSF) Ambizione grant No. 193346. J.O. has been funded by grant No. PID2021-125883NB-C22 by the Spanish Ministry of Science and Innovation/State Agency of Research MCIN/AEI/ 10.13039/501100011033 and by "ERDF A way of making Europe". G.T. acknowledge financial support from project FCE-1-2019-1-156451 of the Agencia Nacional de Investigación e Innovación ANII (Uruguay). The authors thank Joseph DePasquale (STScI) for generating the animation included in the Extended Data.

Contributions J.-Y.L. is the PI of the HST program (GO-16674) to observe the DART ejecta and led the effort to develop this paper. M.H., T.L.F., M.M.K. contributed to the ejecta cone measurement and modeling and ejecta evolution study. G.T. contributed in the photometry, formation of the tail, and the comparison with active asteroids. F.M., A.C.B., B.M., C.O., J.-B.V. contributed in the study of the formation

of the tail. S.C. contributed to photometric study of the ejecta. J.M.S., S.D.R, M.J., C.M.E., and A.M.S. contributed to the understanding of ejecta features related to impact. L.D. and A.V. supported the scheduling, review, and testing of the observing sequence. F.F., S.Ivanovski, A.R., D.J.S., S.S. contributed to dynamical modeling of the ejecta. R.L., D.A.G., T.J.S. supported the derivation of dust size-frequency distribution from dust light scattering properties. A.F.C. and A.S.R. are the DART Investigation Team Lead. N.C. is the DART Coordination Lead. C.A.T. is the lead of the DART Observations Working Group, providing general observations support. E.G.F. is the lead of DART Ejecta Working Group, providing support to the interpretations and modeling of ejecta. N.A.M. supported C.A.T to provide general observations support. S.B., M.G. contribute to the ejecta particle size study. M.T.B., G.C., E.D., R.T.D., E.M.E., I.H., P.H.H., S.Ieva, S.J., T.K., A.L., T.L., Z.-Y.L., P.M., R.M., J.O., M.P., C.S., J.S., P.S., S.R.S., J.M.T.-R., A.F., T.K, T.K, A.M., L.K., F.L.F., M.L., H.W., provided comments and improvements to the manuscript.

Methods

1. Observations and data reduction and processing

We used a total of 19 HST orbits (period 95 min) over about 19 days to observe the Dimorphos ejecta (Extended Data Table 1). The first orbit (orbit 0o) was before impact. The second orbit through the 7th orbit (orbits 01 – 06, yellow in Table 1) started about T+15 min, and continuously observed the ejecta except for the Earth occultation of the target. In the next 5 orbits (orbits 11 – 15, green in Table 1), we observed the ejecta roughly once every 12 hours, and then once every day in the following three orbits (orbits 16 – 18, green in Table 1). In the final phase (orbits 21 – 24, light blue in Table 1) observations were executed once every 3 days. The observations concluded 18.5 days after impact. In each orbit, images were collected at multiple exposure levels, where the central core of Didymos is unsaturated in short exposures, and long exposures saturated Didymos to image the relatively faint ejecta and tail. All images were collected through filter F350LP (pivot wavelength 587 nm, passband rectangular width 480 nm).

The observations were planned to track at the Dimorphos ephemeris rate. This nominally included corrections for parallax due to HST's orbit around the Earth and was expected to keep Didymos inside the field of view with minimal trailing for all exposures. However, due to an as-yet unexplained tracking problem, some orbits lost the target in various numbers of exposures, and some long exposures are trailed by up to more than 10 pixels. We limited our analysis to those exposures with less than 7 pixels of trailing, and occasionally used long exposures with more trailing when no good images were available for the particular orbits.

Images were calibrated by the HST standard calibration pipeline at the Space Telescope Science Institute[30]. We then removed the sky background measured from a square 100 – 400 pixels wide and 100 – 300 pixels from the top right corner, depending on the image size. This area is in general 20" away from Didymos and shows no sign of any ejecta.

Aperture photometry was measured in all short, unsaturated exposures that have been corrected for charge transfer efficiency (CTE; ref) but not geometric distortion (_flc files). The centroid is defined by a 2D Gaussian fit with a 5x5 pixel box centered at the photocenter. The pixel area map was used to correct pixel area variations in the image[30]. The total counts were measured with circular apertures of 1 – 130 pixels radius (0.04" - 5.2"). We converted the total counts to flux density and Vega magnitude based on the photometric calibration constants (PHOTFLAM = 5.3469×10^{-20} erg / (Å cm^2 electron), PHOTZPT = 26.78) provided in the FITS headers and HST photometric calibration website. The total brightness of Didymos including the ejecta and the total brightness of ejecta are shown in Extended Data Fig. 2.

We used the CTE-corrected and geometric distortion corrected images (_drc files) to study the morphology of the ejecta. In order to increase the signal-to-noise ratio of the faint ejecta features, we separately stacked all short exposures and long exposures in each orbit because no change is visible in the ejecta morphology within each orbit. The centroid of long exposures that are saturated in the center was determined by the cross-section of the diffraction spikes. Some trailed long exposures were included in the stack, but those that trailed for more than 10 pixels were discarded. The effects of trailing are accounted for as additional positional uncertainties to the measurements of features, which are mostly smaller than the length of trailing. Cosmic rays and background stars were rejected in the stacking process. Because different numbers of untrailed long exposures were available in each orbit, the total exposure times vary from 25 s – 50 s in most stacked long exposures and reach 155 s for the orbit 21 stack and 110 s for the orbit 23 stack.

Various image enhancement techniques commonly used for studies of comets (see review by ref. 31) were used to assist the identification of ejecta features, including azimuthal median subtraction, re-projection to azimuthal and radial projection, and different brightness stretching and displaying with various color tables. All identified features were cross-confirmed by multiple techniques.

2. Ejecta cone opening angle and direction

We based our ejecta cone characteristics on the ejecta structures moving at >1 m/s in the images within T+8.5 hours (Fig. 1). These structures showed a linear motion moving away from the asteroid along the radial direction (Extended Data Table 2). Assuming that the majority of the ejecta dust is within a thin cone-shaped curtain, the two edges of the cone would appear as two bright rays along the radial direction due to the optical depth effect when viewed from the side. Because the DART impact velocity is close to the sky plane (Extended Data Table 1), if we assume that the cone direction is close to the inverse of the DART impact velocity direction, the cone is close to being viewed from the side in HST images, and the opening angle spanned by the two edges of the cone (linear feature l7 and l8) is close to its 3D opening angle (see below).

We measured the position angles of the two edges of the ejecta cone from both the original image and the enhanced images (see Method S1). The uncertainty range of the position angles is defined by the apparent width of the linear feature. Our measurement resulted in an ejecta cone centered within 5º of the

incoming direction of DART with an opening angle of about 130º. Because of the fuzziness of the ejecta rays and their slight curvature, the uncertainty of the measured position angles could be as high as ±8º, resulting in an uncertainty of the opening angles up to ±12º in some early images. Taking the mean of these two edges and the maximum value of the uncertainty yields the ejecta cone axis at a position angle 67±8° under the assumption that the ejecta cone is axisymmetric along the cone axis.

To test our assumption about the geometry seen from HST in 3D space, we projected a 3D cone geometry onto the HST viewing geometry. We then computed the pixel count peaks from a simulated cone to determine the predicted position angles. Comparing observation-driven peak conditions with numerically derived peaks resulted in a score map that applied a Gaussian distribution-like function to evaluate the consistency. We performed Monte-Carlo simulations by varying the position angles of the observed cone edges within uncertainties to find a best-matched 3D cone geometry. This approach yielded a cone axis direction at (RA, DEC) = (130±10°, 17±12°) and the cone opening angle of 126±14°. Each combination of the cone edges offered two solutions of the cone axis symmetric to the image plane, however, adding uncertainties to the observed edges provided a stochastic distribution of the solutions.

3. Dynamic model of the tail

The position angle of the tail and its uncertainty were determined by the radial directions that define the visible boundary of the tail at the furthest point along the tail in all (short and long exposures) stacked images that contain the tail. The dust dynamics model under the influence of solar radiation pressure follows ref. 15, where the motion of dust is determined by β_{srp}, which is defined as the ratio of the solar radiation pressure force to the solar gravitational force. β_{srp} depends on particle radius, *r*, and density, ρ, as

$$\beta_{srp} = \frac{KQ_{pr}}{\rho r}$$

where K = 5.7x10^{-4} kg/m^2 is a constant, Q_{pr} is the radiation pressure coefficient averaged over the solar spectrum, which is usually assumed to be 1. We assumed a grain density of 3.5x10^3 kg/m^3 for the dust in the ejecta, following the density of ordinary chondrite meteorites[32], considering that Didymos-Dimorphos system shows an S-type spectrum that is associated with (LL) ordinary chondrite material[33].

Pre-impact modeling suggested that the acceleration of solar radiation pressure always exceeds that of the gravitational acceleration of the Didymos system for ejecta particles < 100 μm in size[11,12]. These small particles are pushed out of the binary system in less than 10 hours. Didymos's gravity is predominant within about 3 km for mm particles, and 10 km for cm particles.

The modeling of the orientation of the tail in the sky plane follows the synchrone-syndyne approach[34], where synchrones are the loci of dust particles ejected with zero initial velocity at the same time but with various β_{srp}. The measured position angles of Dimorphos's tail coincide to within 4º of the direction

suggested by the synchrones associated with the time of impact in all images, suggesting that solar radiation pressure dominates the tail formation (Extended Data Fig. 4). The small discrepancy between T+1 and T+5 days is likely due to the slight apparent curvature of the tail (Fig. 3h).

The non-zero initial velocity of ejecta dust causes the tail to be widened towards the direction of the velocity when the particles escape the Didymos system. The average initial velocity of Dimorphos's ejecta, as projected in the image plane, can be decomposed into a sunward component and a northward component, and the latter causes the widening of the tail toward the north. The relatively sharp southern edge and the more diffuse northern edge are consistent with the expectation from the ejecta mass-speed relationship[35]. The 1" width of the tail is consistent with a velocity dispersion Δv = 0.15 m/s, comparable to or slightly smaller than the orbital velocity of Dimorphos, suggesting that the tail is primarily composed of the slowest ejecta.

The inverse proportionality of β_{srp} with particle size means that small particles experience stronger solar radiation pressure and are pushed away from the asteroid faster after ejection than large particles. Because the duration of our HST observations is much shorter than the orbital period of Didymos around the Sun (2.1 years), the motion of particles along the tail relative to the asteroid under solar radiation pressure can be approximated by a constant acceleration motion. As the length of the tail grows, particles of various sizes spread out along the tail, with the smallest particles remaining near the far end of the tail from the asteroid, while larger particles dominate the end near the asteroid. Assuming a power-law differential particle size distribution with an exponent of α for the tail, we derived that the brightness of the tail is expected to have a power-law relationship with the distance to the asteroid with an exponent b = -4 - α.

We extracted the brightness profiles of the tail from stacked long exposures from T+5 hours until the last stack at T+18.5 days (Extended Data Fig. 5). The exponent α of the particle size distribution was derived from the linear part of the tail brightness profiles (in log-log space) in various images, corresponding to a range of β_{srp} from 0.2 to 8×10^{-4}, to be nearly constant with an average of -2.6 and a standard deviation of 0.2. The range of β_{srp} indicates particle sizes between about 1 μm and a few mm. In images after about T+6 days, the tail brightness displays two regions with different power law slopes. The inner region appears to be influenced by the particles in the spirals that started to overlap with the tail. The outer region has best-fit slopes close to -2.6 as in the early images, whereas the slope of the inner region ranges from -3.4 to -3.75. The range of β_{srp} for the inner region is 7×10^{-4} to 1×10^{-5}, corresponding to the large mm – cm sized particles. The lack of small particles in the spirals is expected because 100 μm or smaller particles should have been removed a few hours after impact. The apparent increasing steepness of the particle size frequency distribution in this size range also seems to indicate that the bulk of ejecta particles have a size cutoff at a few cm. If the particle size frequency distribution of the tail represents that of the ejecta, then a power law index of -2.6 means the total ejecta mass is dominated by the largest particles.

The above treatment assumes that the albedo is independent of particle size, which needs to be examined. Based on laboratory phase function measurements of micron-size aerosols[36] and mm-size particles[37], along with supporting models of scattering efficiency[38], the albedo of μm-size particles is about 70% that of mm-grains at the phase angle of our early observations (54º). This brightness ratio is reversed at the phase angle corresponding to the final images (74º), where μm-size particles become about 16% brighter. Our calculation suggests that the small difference between the albedos of μm- and mm-sized particles changes the best-fit power law index of the particle size frequency distribution by less than 2%. Our assumption of the same albedo throughout the μm- to cm sized particles holds.

4. Secondary tail

The small decrease of the overall fading rate of the the Didymos system total brightness between about T+5 and T+7 days indicates an increase in the total scattering cross-section in the ejecta within 10 km of the system (Extended Data Fig. 2), partly compensating for the ejecta moving out of the photometric aperture. It is unlikely to be caused by albedo change for the ejecta particles. Injection of new dust particles into the ejecta is considered.

This scenario and its timing is also supported by the synchrone model (Extended Data Fig. 6), where the projected direction of the secondary tail is consistent with the synchrones associated with about T+5 to T+7 days. The similar narrow width of the secondary tail with the original tail suggests a low initial velocity of ~0.15 m/s for the dust particles. While the Didymos binary environment could complicate the dust motion and cause deviation from the zero initial velocity assumption of the idealized synchrone model, the observed low initial velocity of the dust in the secondary tail implies limited effects.

The possible mechanisms of the secondary dust emission could include the re-impact of ejecta blocks onto Dimorphos or Didymos[12], or large ejecta blocks disintegrating into small pieces due to spin up or mutual collisions[39]. Mass shedding from the surface of Dimorphos due to rotation is not likely given its slow rotation if its spin is tidally locked. But mass movement and shedding from Didymos could potentially be triggered by ejecta re-impact due to its fast rotation causing a net outward acceleration at its equator[40], though no clear indication has been confirmed yet[25]. Once dust is lifted from the surface of Dimorphos or Didymos via these mechanisms, solar radiation pressure will quickly sweep the dust into the antisolar direction, forming a secondary tail.

Other mechanisms, such as the dynamic interaction between the slow ejecta dust and the binary system[11], gravitational scattering for the ejecta dust when they are turned back by solar radiation pressure and pass the binary system, or photon-charged dust particles under the influence of interplanetary magnetic field[41] could also result in unusual tail morphology leading to the appearance of a secondary tail. But they may not be accompanied by the increase of ejecta dust as suggested by the fading lightcurve of the Didymos system.

Methods References

30. Sahu, K., et al. WFC3 Data Handbook, Version 5.0, Baltimore: STScI https://hst-docs.stsci.edu/wfc3dhb (2021).
31. Samarasinha, N.H., Larson, S.M. Image enhancement techniques for quantitative investigations of morphological features in cometary comae: A comparative study. *Icarus*, **239**, 168-185 (2014).
32. Britt, D. T. & Consolmagno, G. J. Stony meteorite porosities and densities: A review of the data through 2001, *Meteoritics & Planetary Science*, **38**, 1161-1180, doi:10.1111/j.1945-5100.2003.tb00305.x. https://doi.org/10.1111/j.1945-5100.2003.tb00305.x (2003).
33. Dunn, T. L., Burbine, T. H., Bottke, W. F. & Clark, J. P. Mineralogies and source regions of near-Earth asteroids, *Icarus*, **222**, 273-282. doi:10.1016/j.icarus.2012.11.007. https://doi.org/10.1016/j.icarus.2012.11.007 2013).
34. Finson, M. J. & Probstein, R. F. A theory of dust comets. I. Model and equations, *Astrophysical Journal*, **154**, 327-352 https://dx.doi.org/10.1086/149761(1968).
35. Fahnestock, E. G., Cheng, A. F., Ivanovski, S., Michel, P., Raducan, S. D. et al. Pre-encounter Predictions of DART Impact Ejecta Behavior and Observability, *Planetary Science Journal*, **3**, 206 https://doi.org/10.3847/PSJ/ac7fa1 (2022).
36. Volten, H., Muñoz, O., Rol, E., de Haan, J. F., Vassen, W. et al. Scattering matrices of mineral aerosol particles at 441.6 nm and 632.8 nm, *Journal of Geophysical Research: Atmosphere*, **106**, D15, 17375-17401, doi:10.1029/2001JD900068, https://doi.org/10.1029/2001JD900068 (2001).
37. Muñoz, O., Moreno, F., Vargas-Martín, F., Guirado, D., Escobar-Cerezo, J., Min, M. & Hovenier, J. W. Experimental Phase Functions of Millimeter-sized Cosmic Dust Grains, *The Astrophysical Journal*, **846**, 1. doi:10.3847/1538-4357/aa7ff2, https://doi.org/10.3847/1538-4357/aa7ff2 (2017).
38. Nousiainen, T., Kahnert, M. & Lindqvist, H. Can particle shape information be retrieved from light-scattering observations using spheroidal model particles? *Journal of Quantitative Spectroscopy and Radiative Transfer*, **112**, 13, 2213-2225, doi:10.1016/j.jqsrt.2011.05.008. https://doi.org/10.1016/j.jqsrt.2011.05.008 (2011).
39. Ivanovski et al. submitted to *Planetary Science Journal*.
40. Hirabayashi, M., Ferrari, F., Jutzi, M., Nakano, R. and Raducan, S. D. Double Asteroid Redirection Test (DART): Structural and Dynamic Interactions between Asteroidal Elements of Binary Asteroid (65803) Didymos, *The Planetary Science Journal*, **3**, 140, doi:10.3847/PSJ/ac6eff. https://doi.org/10.3847/PSJ/ac6eff (2022).
41. Hartzell, C. M. Dynamics of 2D electrostatic dust levitation at asteroids, Icarus, 333, 234-242, doi:10.1016/j.icarus.2019.05.013. https://doi.org/10.1016/j.icarus.2019.05.013 (2019).
42. Kitazato, K., Abe, M., Mito, H., Tarusawa, K., Soyano, T. et al. Photometric behaviour dependent on solar phase angle and physical characteristics of binary near-Earth Asteroid (65803) 1996 GT, In *Lunar Planetary and Science*, **35**, 1623. https://ui.adsabs.harvard.edu/abs/2004LPI....35.1623K/abstract (2004).

Figures

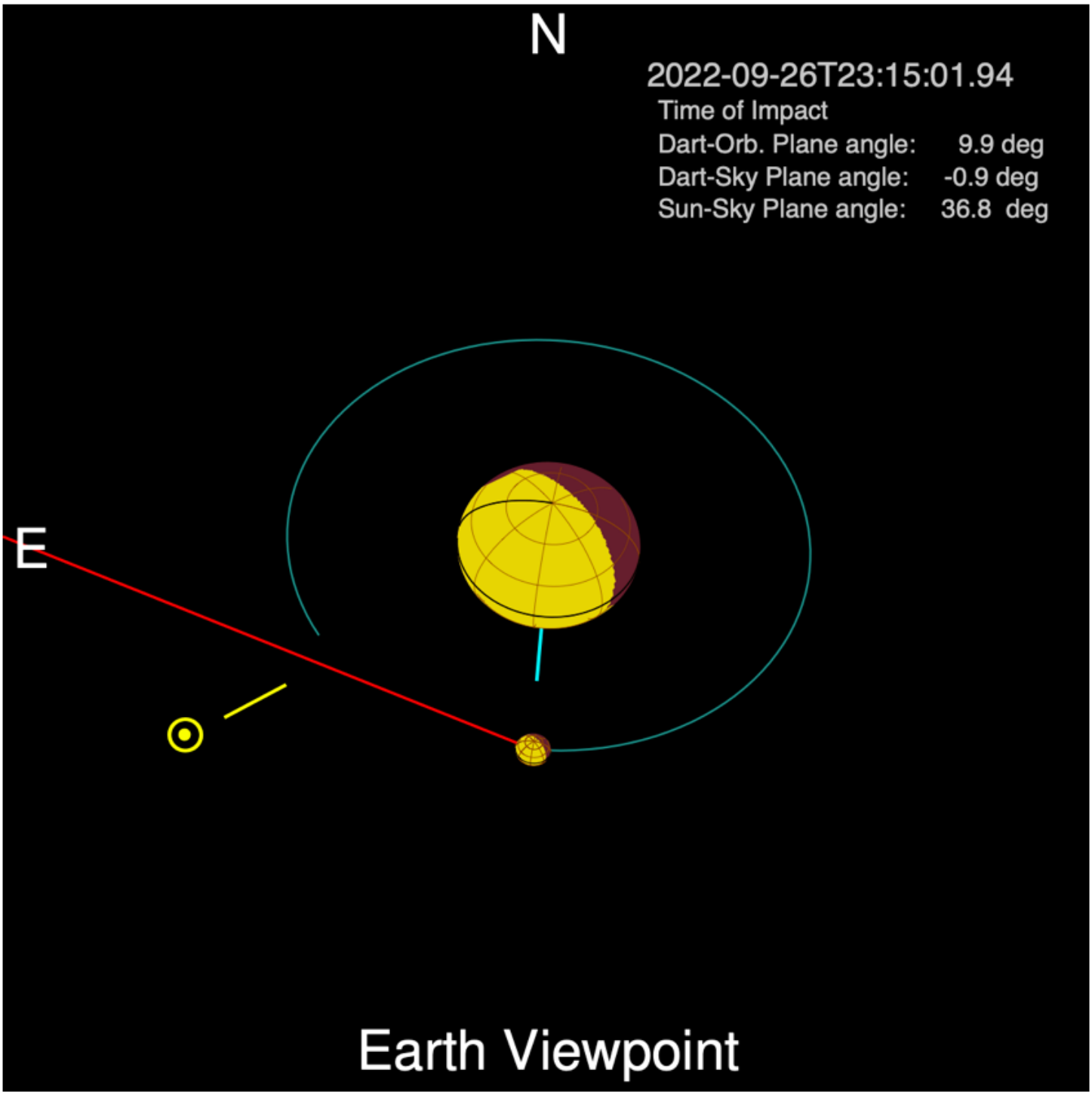

Figure 1

Geometry of the Didymos system at the time of impact as viewed from the Earth. Sky north is in the up direction and east is on the left in this view. Didymos is the large spheroid in the center. Dimorphos is the small spheroid orbiting Didymos in the orbit represented by the green circle, moving clockwise at an orbital speed of ~0.17 m/s. The positive pole of Didymos (also the orbital pole of the system) is represented by the cyan line, pointing close to the south celestial pole and 51° out of the sky plane away from the Earth. The Sun is at a position angle (angle from north toward east) of 118°, represented by the

yellow line and dot-circle symbol. The DART spacecraft vector at impact is represented by the red line, going from east to west at a position angle of 68° and within 1° of the sky plane.

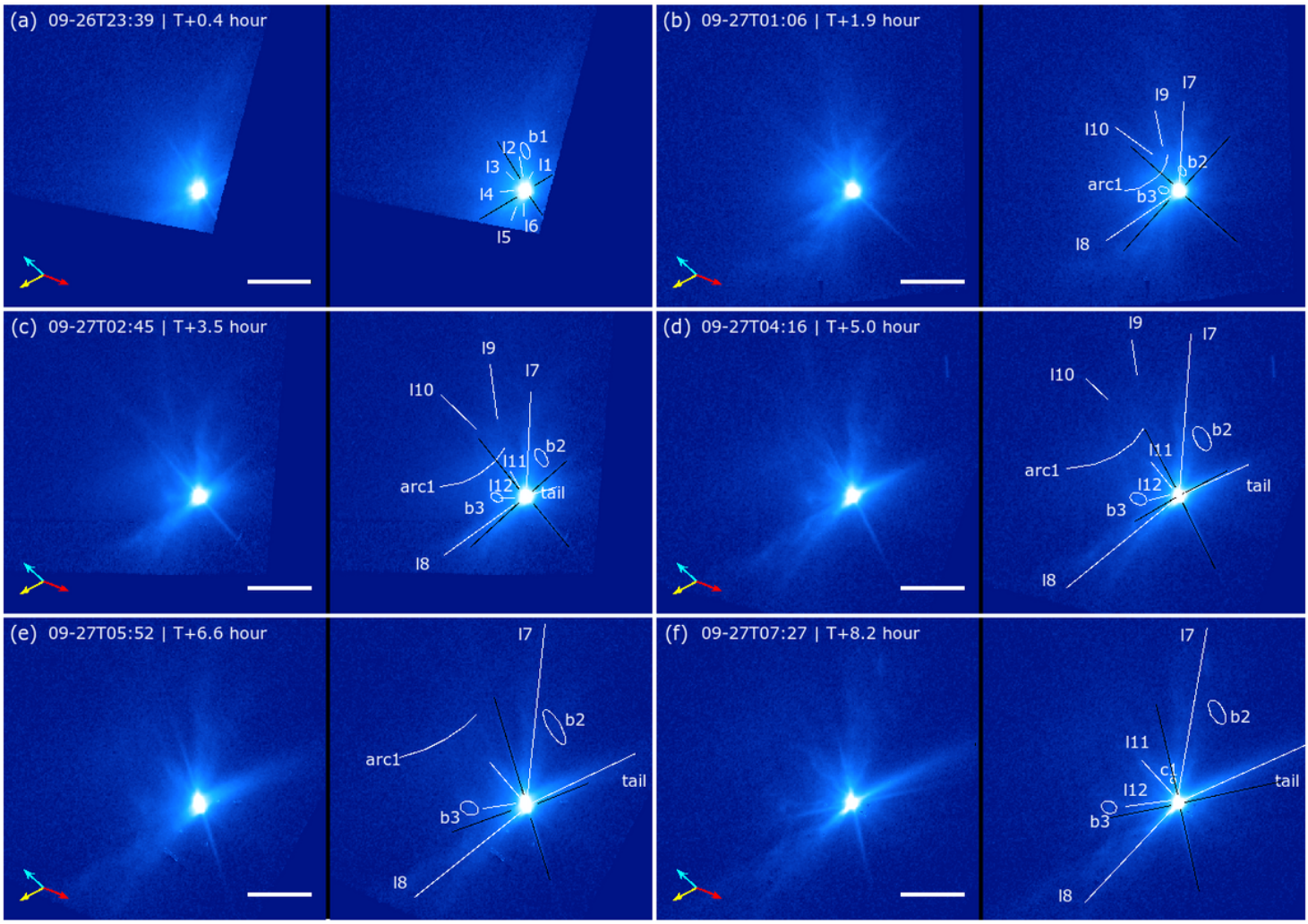

Figure 2

Evolutionary sequence of Dimorphos ejecta from T+0.4 to T+8.2 hours. All images are displayed in duplicate pairs, with the left unannotated and the right having features marked by white markers and names. The times correspond to the mid-observation time of each image. Black lines mark diffraction spikes from the instrument. All images are displayed with the same logarithmic brightness stretch. Sky north is in the up direction and east to the left. The scale bars mark 200 km at the distance of Didymos. The yellow arrows point to the direction of the Sun, the cyan arrows the heliocentric orbital velocity direction of Didymos, and the red arrows the direction of DART spacecraft at impact, all projected in the sky plane at the time of observations. The first four images (T+0.4 to T+5.0 hour) are trailed for 4 – 7 pixels, and the T+6.6 hours image is trailed for 14 pixels, all along the northeast-southwest direction (see Methods). The trailing widens the tail and the two diffraction spikes in the orthogonal direction. Most features are much larger than the length of trailing, and we added uncertainties to account for the effect of trailing in our measurements. Many features are visible during this period, including linear features (l1

– l12), an arc feature (arc1), a circular feature (c1), blobs (b1 – b3), and a tail. The ejecta cone is marked by linear features l7 and l8.

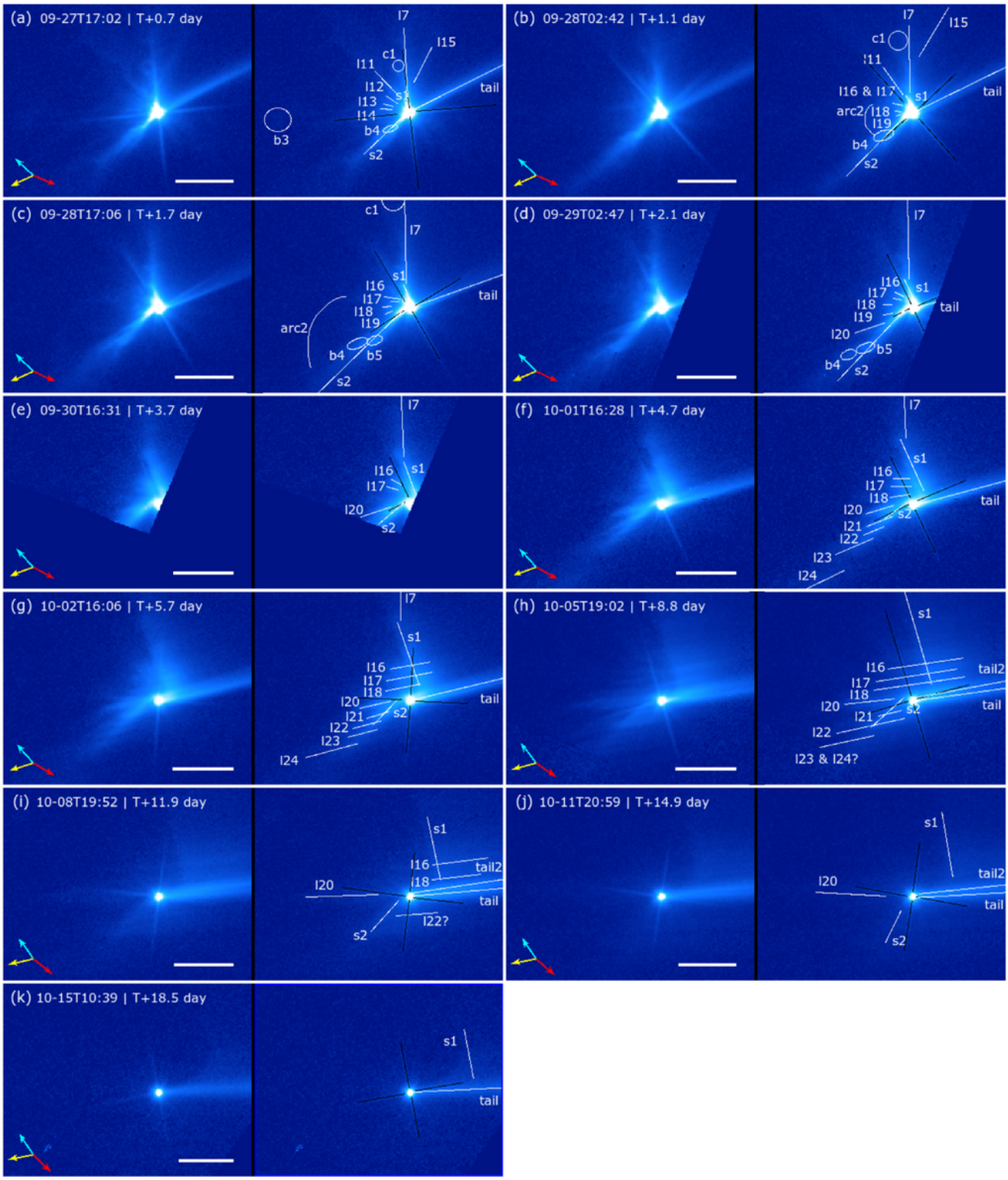

Figure 3

Evolution of ejecta from T+0.7 days (T+17.8 hours), following Figure 1, through T+18.5 days. The image orientation, brightness stretch, scale bars, and vector arrows are all the same as in Fig. 2. The main

characteristics of the ejecta during this period of time include the spirals (s1 and s2), linear features (l7, l11 – l24), blobs (b3 – b5), a circular feature (c1), and an arc (arc2). The original ejecta cone (l7) is still visible in images before T+5.7 days (panels a – g). The early southern spiral (s2) could be overlapped with the south edge of the original ejecta cone (panels a – e), which is not separately marked. The northern spiral (s1) is widened along the tail direction in about T+5 days, forming a wing-like feature (panels g – k). A group of linear features (l16 – l24), some being part of the southern spiral (l21 – l24), showed a clockwise rotation about Didymos from T+1.1 to T+4.7 days (panels b – f). These linear features later (T+5.7 days) stretched along the tail direction under solar radiation pressure (panel g – i), with those in the north of Didymos overlapping with the wing-shaped feature. A secondary tail is visible between T+8.8 and T+14.9 days (panels h – j, also see Fig. 4). The curved edge of the wing-like feature is visible in the last image (panel k).

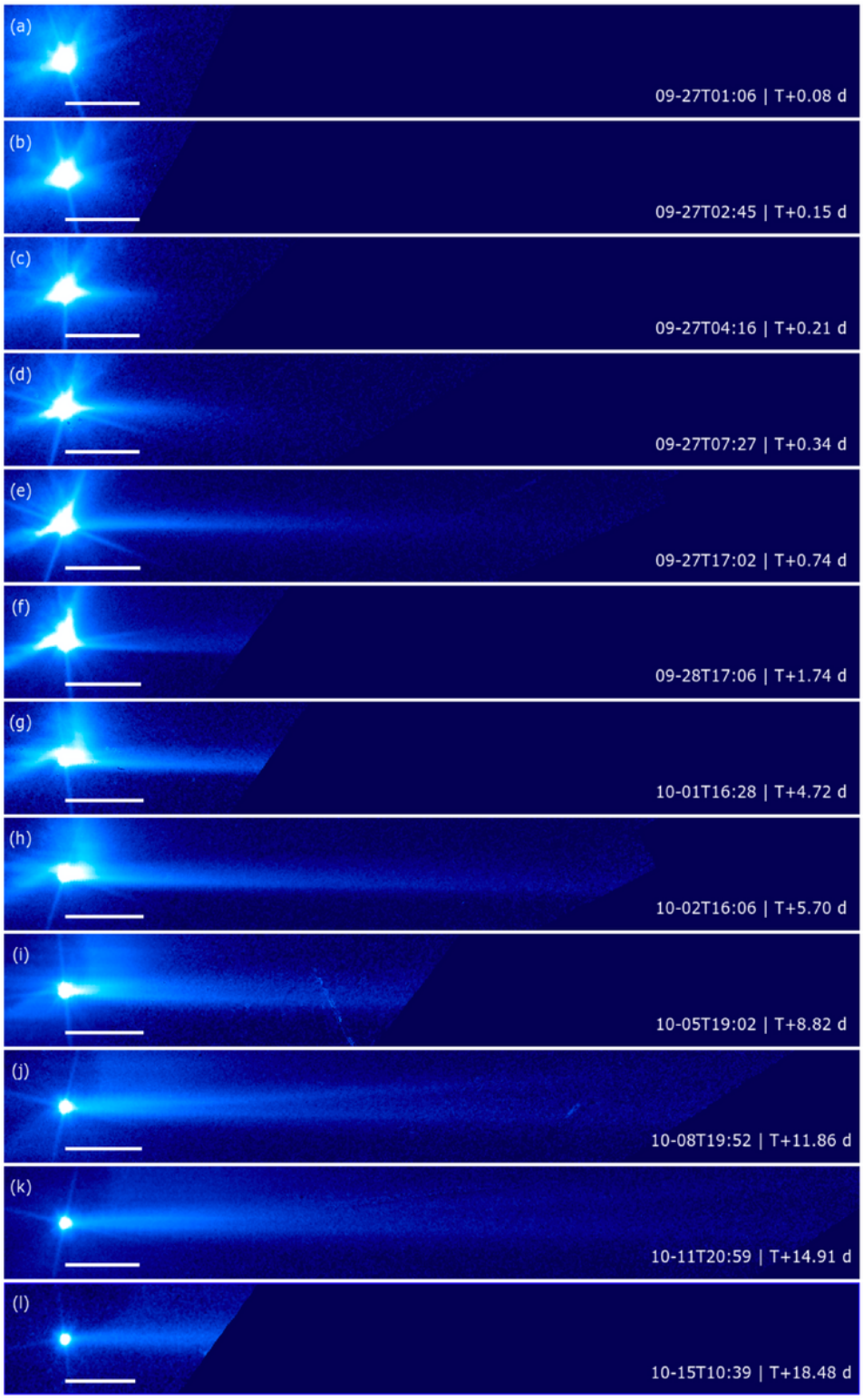

Figure 4

Tail formation from the Dimorphos ejecta cloud. All frames are rotated such that the expected direction of the tail based on our dust dynamic model (see text and supplementary material) is in the horizontal direction extending towards the right. All frames are displayed in the same logarithmic brightness scale. The scale bars are aligned with the asteroid on one end and extend 200 km long towards the tail direction. Note that the first three frames (a, b, c) are trailed 5 – 7 pixels approximately along the direction

of the vertical diffraction spikes. The trailing in all other frames is < 2 pixels. The first frame (a) in this sequence acquired at T+0.08 days (T+1.9 hours) shows no signs of a tail. A tail was visible starting from the second frame (b) acquired at T+0.15 days (T+3.5 hours). The tail continued to grow in a direction that is in general consistent with an impulsive emission of dust from Dimorphos at the time of impact. The secondary tail is visible between T+8.82 and T+14.91 days (panels i – k), pointing at about 4º north of the original tail.

Supplementary Files

This is a list of supplementary files associated with this preprint. Click to download.

- DARTejectavideo.gif
- ExtendedOnlineData.docx